ADVANCED FUNCTIONAL MATERIALS
www.afm-journal.de

Enhanced Magnetic Anisotropy for Reprogrammable High-Force-Density Microactuators

Yulan Chen, Karthik Srinivasan, Marcus Choates, Ludovico Cestarollo, and Amal El-Ghazaly**

The precise control of magnetic properties at the microscale has transformative potential in healthcare and human-robot interaction. This research focuses on understanding the magnetic interactions in nanostructure assemblies responsible for microactuation. By combining experimental measurements and micromagnetic simulations, the interactions in both nanocube and nanochain assemblies are elucidated. Hysteresis measurements and first-order reversal curves (FORC) reveal that the spatial arrangement of these assemblies governs their collective magnetism. A critical concentration threshold is observed where a transition from ferromagnetic-like to antiferromagnetic-like coupling occurs. Leveraging the high uniaxial anisotropy of 1D nanochains, the remanent magnetization of assembled chain structures is maximized for efficient magneto-mechanical energy transduction. By utilizing an optimized magnetic nanostructure concentration, a flexible film is fabricated, and its significantly enhanced mechanical deformation response to a small magnetic field, surpassing conventional particle-based samples by a factor of five, is demonstrated. Demonstrating excellent transduction efficiency, visible deformations such as bending and S-shaped twisting modes are achieved with an applied field of less than 400 Oe. Furthermore, the reprogrammability of the actuator, achieving a U-shaped bending mode by altering its magnetization profile, is showcased. This research provides valuable insights for designing reconfigurable and effective microactuators and devices at significantly smaller scales than previously possible.

1. Introduction

Magnetic actuation is flourishing as the preferred mode of actuation in a number of new devices and technological systems, including soft robots,[1,2] tactile displays,[3,4] mechanical metamaterials,[5,6] and minimally invasive medical devices.[7,8] The advantage of magnetic actuation arises from the fast response time to external magnetic fields and the large design space for magnetic programming of the actuation behavior. By preprogramming local magnetic clusters (referring to regions formed by agglomerates of many particles) inside a soft polymer body, an applied magnetic field can induce sufficient forces or torques on the magnetic clusters and thereby deform the body in the prescribed directions.[9] In the design of these magnetic actuation systems, although significant effort has been put forth to investigate the choice of the magnetic fillers,[10,11] their spatial arrangement in the soft matrix,[12] and the techniques to reprogram their magnetization profiles,[13] magnetic actuators are still limited in terms of miniaturization, efficiency, and reprogrammability.

Magnetic fillers widely used in the literature include spherical shaped magnetic particles (such as iron oxide[14,15] and NdFeB[16,17]) that lack shape anisotropy and thus require a high loading of magnetic material or the use of strong fields to achieve a noticeable response. In order to achieve significant actuation and effective transduction of magnetic field energy into mechanical energy, it is important to have a high remanent magnetic moment. This is because a high remanent magnetic moment can produce a substantial magnetic force ($\vec{F} = \nabla(\vec{m} \cdot \vec{B})$) or torque ($\vec{\tau} = \vec{m} \times \vec{B}$) even with a small field. Consequently, the focus has shifted toward the preferential alignment of magnetic fillers within polymer matrices, which offers not just heightened remanent moment but also precise control over the movement and actuation of flexible shape-morphing systems.[18] Common strategies for producing anisotropic magnetic elastomers involve first mixing particles into the elastomer, followed by using a large external magnetic field to align particles into long strands extending horizontally over tens of micrometers.[19–24] Recent advancements in this field have been achieved by Kim et al.,[25] who designed an

Y. Chen, L. Cestarollo
Department of Materials Science and Engineering
Cornell University
Ithaca, NY 14853, USA
E-mail: yc2555@cornell.edu
K. Srinivasan, A. El-Ghazaly
Department of Electrical and Computer Engineering
Cornell University
Ithaca, NY 14853, USA
E-mail: ase63@cornell.edu
M. Choates
Department of Materials Science and Engineering
The Pennsylvania State University
State College, PA 16801, USA

The ORCID identification number(s) for the author(s) of this article can be found under https://doi.org/10.1002/adfm.202305502

DOI: 10.1002/adfm.202305502

optofluidic maskless lithography system. This approach employs photopatterning to write spatially-varying magnetic anisotropy into magnetic actuators, thereby enabling pre-programmed motion at the microscale.

Another challenge with magnetic fillers is that these particles tend to aggregate and agglomerate due to various types of particle–particle attractions, including magnetic dipolar forces, van der Waals forces, or the surface chemistry mismatch between the inorganic material and the polymer matrix.[26,27] Since the particles were initially aggregated in different-sized clusters before the magnetic field was applied, the resulting actuators feature elongated magnetic strands with a broad distribution in widths spanning tens of micrometers. As the body size of these actuators is scaled down to the length scales of a biological cell (<100 μm), the magnetic clusters must undergo a similar reduction in size, ideally reaching dimensions on the order of several micrometers or even smaller. In such a context, any agglomeration of particles together degrades the actuator's resolution because the magnetic filler becomes bulkier than the desired bending radius.

Further enhancement in the magnetic response in such nanocomposites is not feasible by simply loading more particles into the polymer matrix.[28] This is due to the fact that upon reaching a certain volume concentration, or percolation threshold, particles in densely packed clusters begin to experience long-range interactions. Though many models exist to explain how densely packed nanoparticle assemblies undergo a phase transition from a superparamagnetic state to a superspin glass state at low temperatures, characterized by a decrease in relaxation time, this has been reported for systems with superparamagnetic particles smaller than 20 nm.[29–33] The authors are unable to model the particle interactions in this work using superspin glass behavior since here the particles are around 100 nm in size and exhibit ferromagnetic behavior at room temperature. The absence of superspin glass behavior can be attributed to two essential elements missing from this nanoparticle system: long-range magnetic disorder and magnetic frustration.[34] Rather, in systems of ferromagnetic particles, depending on the orientation, local magnetic dipolar interactions can cause ferromagnetic head-to-tail coupling and increase the net remanent magnetization; or, in other orientations, the dipolar interactions between adjacent elements encourage an antiparallel (also termed "antiferromagnetic-like") alignment of the magnetization, which consequently reduces the net remanent magnetization and the mechanical response to a field.[35]

To effectively miniaturize these magnetic clusters while preserving their remanence, it is worth considering that optimizing performance in micromagnetic actuators could potentially be achieved by employing structures that feature their smallest dimension within the nanometer range and their largest dimension within the micrometer range. This approach contrasts with the prevailing usage of elongated magnetic strands, in which both dimensions span across micrometers, as often observed in existing literature.[36,37] By significantly reducing one of the dimensions to a sub-micrometer, the potential arises for substantial increases in aspect ratios, subsequently leading to a large rise in remanence. Previous studies have investigated the incorporation of high-aspect-ratio magnetic fillers, such as spindle-type particles,[38] nanowires,[39] and nanochains,[40] into polymer matrices to achieve complex actuations with large deflection and shape control. Both experimental and computational investigations on 1D magnetic chains have confirmed that they exhibit enhanced remanent magnetization (in the direction of the long axis), clearly distinct from the properties of individual magnetic nanoparticles.[41–46] Despite their potential as desirable anisotropic magnetic fillers in high-force-density actuators, the microscale arrangements and collective magnetic behaviors of 1D magnetic chains in a polymer matrix are yet to be investigated in great detail.

In the current work, we performed an in-depth study to uncover the correlation between microscale arrangements of FeCo magnetic nanocubes (MNCs) and nanochains,[47] as well as their collective magnetic behaviors in MNC strand assemblies and elongated nanochains. The distinction between these structures is illustrated in **Figure 1**, where the building blocks and their corresponding assemblies are depicted within the same rectangles, colored purple and yellow, respectively. Within the purple rectangle in Figure 1, nanocube strands are assembled by drop casting a solution of individual MNCs. In contrast, nanochains and elongated chains (yellow rectangle in Figure 1) are formed by drop casting structurally connected nanocubes, which have been synthesized together to form a continuous chain. We focused on understanding the interplay between filler shape and assembly structure and their impact on the global, that is, net magnetic anisotropy and net remanent magnetization. These factors significantly affect the mechanical response and are crucial in designing reprogrammable microactuators. For comparison, such relationships have also been investigated in randomly-oriented MNCs and nanochains. Scanning electron microscopy (SEM) studies offer direct visualization of the arrangements of the 1D chains in the larger arrays and verify that the chains are single-nanocube-wide, making them ideal unit cells for studies of magnetic remanence and coercivity as a function of packing density and chain aspect ratio. We studied the arrangement of chains as a function of lateral distance between them (volume percentage of chain solution) and how variable lateral dimensions of chains (length and aspect ratio) correlate with dipolar interactions, which have not been fully understood. The net uniaxial magnetic anisotropy was investigated through the measurement and simulation of hysteresis loops, along with the analysis of FORC. The change in global magnetism occurs as a direct result of the local change in magnetic interactions. Disambiguated in Figure 1, the concepts of inter-cube/chain interactions have been used for the theoretical interpretation of such changes. Finally, we fabricate a magnetic actuator with the 1D optimal array density to achieve maximum magnetic remanence of the composite and yield the efficient magneto-mechanical transduction for enhanced actuation of 380 μm in a field of 1000 Oe (100 mT). Thus, this extensive analysis of both local nanoscale fabrication and global magnetic behavior can provide the insight needed to greatly extend the capabilities of magnetic actuators with micrometer-scale features and control.

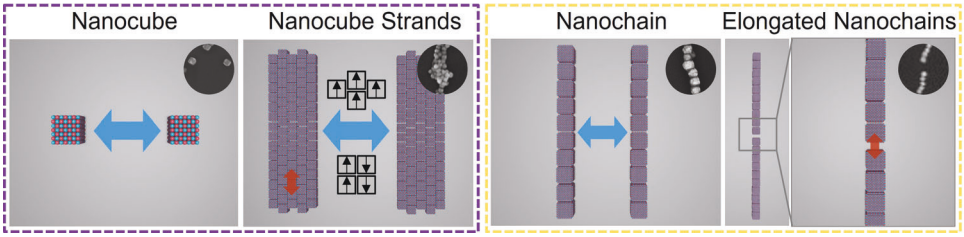

Figure 1. Schematic illustration of the assembly structures under investigation, formed from magnetic nanocubes (left) and chains (right) in external magnetic fields, and the long-range (blue arrows) as well as short-range (red arrows) inter-cube/chain interactions within the assemblies.

2. Results and Discussion

2.1. Structural Properties of the Nanocubes and Nanochains

FeCo MNCs were synthesized by the widely-used ethylene glycol method resulting in MNCs with diameters around 150 nm (**Figure 2**A). Using our recently-developed method,[47] FeCo nanochains were synthesized into assembled chains without the use of an externally-applied magnetic field. As shown in Figure 2A, randomly-oriented anisotropic structures of chains can be observed; in each chain, the MNC building blocks are connected structurally, appearing to grow onto each other to form the chain, as seen from the bright-field transmission electron microscopy (TEM) image in Figure 2B. The dark color contrasts uniformly observed throughout the chain further confirm its purely metallic nature. This pure magnetic chain structure provides the advantages of enhanced conductivity and magnetic anisotropy along the length of the chain, as opposed to most studies, where there are slight gaps between the building blocks due to a non-conductive inorganic or organic coating to the individual MNCs.[48,49]

The energy dispersive X-ray spectroscopy (EDS) spectrum for the FeCo loose MNCs indicates that they consist of FeCo, with a composition of Fe (65.10 at%) and Co (34.90 at%). The EDS spectrum for the FeCo nanochains reveals a similar composition ($Fe_{65}Co_{35}$). The crystal structure of both the MNCs and chains was confirmed by X-ray diffraction (XRD). Figure S1, Supporting Information, demonstrates that the major diffraction peaks

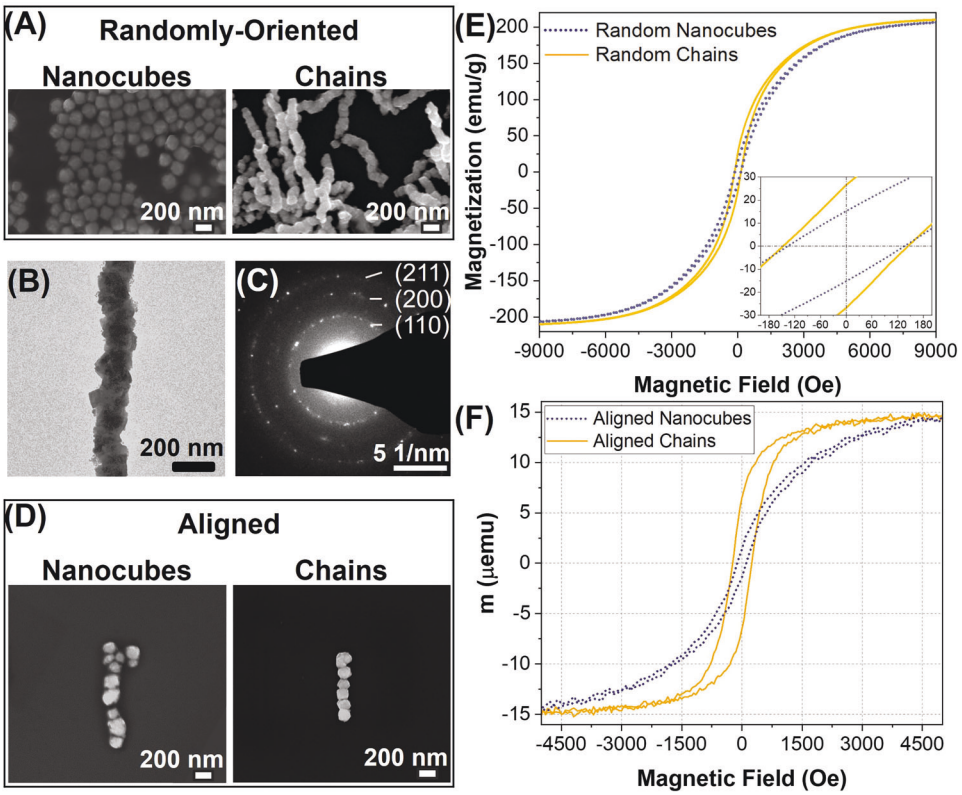

Figure 2. A) SEM images for randomly-oriented FeCo nanocube and chain samples; B) TEM image of a representative FeCo chain with C) SAED pattern showing the bcc FeCo alloy (110), (200), and (211) Bragg reflections; D) SEM images for the dilute concentrations of magnetically aligned nanocube and chain samples. E) Magnetic hysteresis loops for samples (Inset: zoomed-in loops from −200 to 200 Oe); and F) magnetic hysteresis loops for the corresponding magnetically aligned nanocube and chain samples measured with the applied field parallel with the long axis.

match well with the standard data for a bulk body center cubic (bcc) FeCo alloy (JCPDS Card No. 49-1567), which can be identified by the (110), (200), and (211) reflections. Narrow and well-defined diffraction peaks indicate the high crystallinity of the synthesized nanostructures. Despite minor variations in the peak width, there are no significant differences between the two spectra. It is worth mentioning that the $CoFe_2O_4$ phase, which usually accompanies FeCo alloys because of oxidation, is present in such small amounts that it does not appear in the XRD spectra. As a result, we do not expect an antiferromagnetic exchange contribution to the magnetic behavior from the CoO and have confirmed this by measuring the low temperature hysteresis of the sample in Figure S4, Supporting Information. The selected area electron diffraction (SAED) pattern (Figure 2C) of the FeCo chain indicates the prominent FeCo bcc phase with the (211), (200), and (110) planes whose *d*-spacings agree with those from the XRD analysis. (More information about SAED analysis can be found in Table S1, Supporting Information).

2.2. Magnetic Properties of the Randomly-Oriented Nanocubes and Chains

Figure 2E shows hysteresis loops of randomly-oriented MNC and chain samples at 300 K up to ± 9000 Oe. Both structures have the same saturation magnetization values as the bulk material M_s = 220 emu g^{-1} at room temperature and have a non-zero remanent magnetization. Although the coercive field is low (H_c < 150 Oe) for all samples, a clear improvement in the remanent magnetization can be seen in the nanochains. The remanent magnetization for the MNCs is 15 emu g^{-1}, which is in agreement with the data in the literature.[50,51] Thus, the ratio of remanent magnetization to saturation magnetization, M_r/M_s, is only 0.068 in the MNCs. In contrast, the randomly-oriented FeCo chain sample exhibits a remanent magnetization of M_r = 28 emu g^{-1} and M_r/M_s ratio of 0.127, which is almost twice that of FeCo MNCs. Such a significant enhancement in remanent magnetization is often observed for anisotropic magnetic structures and is usually ascribed to the increased shape anisotropy creating a preference for the magnetization to lie along the length of the structure.

2.3. Magnetic Properties of Aligned Nanocubes and Aligned Chains

To achieve directional and selective actuation, the concentration and orientation of the magnetic clusters within the polymer matrix must be predetermined during the fabrication process. While the concept of using magnetic fields to orient the magnetic clusters has been long established, the local structure-property relationships in such materials have not been extensively quantified experimentally and optimized for use in actuators. The response of the assembled clusters to an externally applied field is strongly influenced by the magnetic interactions between them. Further, it is not clear how hysteresis loops evolve when interactions between magnetic clusters dominate over their response to an external field and how this evolution determines the mechanical response. Therefore, understanding the role of magnetic interactions in these assembled structures is crucial for shape morphing. Interactions in assemblies can be categorized as either long-range, which has been studied here by varying the nanocube/chain concentration, or short-range, which can be controlled to some extent by changing the size of or adding spacers around the nanocubes/chains (not studied here).[52] As depicted in Figure 1, the nature and strength of interactions depend on the nanocubes/chains' arrangement, and on the lateral distance between them.

Table 1. Magnetic properties of aligned FeCo nanocube and chain samples.

Sample	Coercivity ($H_{c\|\|}$)	Remanence ($M_{r\|\|}$)	Normalized remanence ($M_r/M_{s\|\|}$)
Aligned nanocube	126.7 Oe	1.3 μemu	0.09
Aligned chain	250.8 Oe	6.2 μemu	0.43

Samples with uniformly-aligned FeCo MNCs or chains were prepared via the method of drop casting (see Figure S2, Supporting Information), and their magnetic properties were measured. Starting from the assembled structures with minimum interactions, dilute solutions (0.5 vol%) of either MNC or chains were deposited onto silicon wafers in the presence of a magnetic field of 100 mT. As clearly depicted in SEM images of Figure 2D and Figure S3, Supporting Information, the magnetic field strength was sufficient to successfully impose the alignment of the nanostructures along the field lines. Though both sets of nanostructures demonstrate a strong degree of directionality, clear differences arise. The MNCs tend to form very short chains (in the range of 1 μm), and some even aggregate into larger clusters with widths of three nanocubes (left in Figure 2D). These clusters subsequently attract other isolated nanocubes. As a result, the side width of the MNC strand has a broad distribution. On the other hand, the nanochains exhibit an extremely narrow distribution in widths, as displayed in Figure 2D. Even when stacked, the chains tend to attract each other end-to-end instead of side-by-side, resulting in longer chains with a width equal to only one nanocube side length. It is worthwhile to mention that this unique structure helps to minimize the unfavorable interaction that degrades remanent magnetization (deteriorates switching behaviors and, in turn negatively affects the resolution of actuation), which will be confirmed in the following magnetic characterization.

The hysteresis loops measured for both the aligned MNC strands and chains are shown in Figure 2F and the key magnetic parameters are reported in **Table 1**. Comparing the hysteresis loop of the aligned MNCs (Figure 2F) with that of the randomly-oriented MNC sample (Figure 2E), we observed a similar H_c value (126.7 Oe) and a 28% increase in M_r/M_s (to 0.087) for the aligned MNCs. Compared to this meager increase in remanence for MNCs, the 0.5 vol% aligned magnetic chain sample, on the other hand, showed much more significant enhancements in H_c and M_r/M_s values— both values doubled. As indicated by the more square hysteresis loop and the values in Table 1, the remanent magnetization of the aligned nanochain sample approaches half the saturation magnetization.

The magnetic behavior of randomly-oriented versus aligned samples of nanocubes or chains can be explained through an analysis of the inter-cube/chain interactions. Previous studies have shown that interactions always suppress coercivity.[53,54]

However, the impact of these interactions on the remanence of the sample varies based on the alignment. Specifically, a ferromagnetic-like configuration enhances the remanent magnetization, while an antiferromagnetic-like configuration results in reduced remanent magnetization. Our measurements of coercivity and remanent magnetization support this finding.

The comparable coercivity values of the randomly-oriented and aligned nanocube samples suggest that the magnetic interactions between nanocubes are equally strong in both cases, despite the different degrees of order leading to varying remanence values. In the 0.5 vol% aligned MNC sample, the elongated structure induces uniaxial shape anisotropy, which helps increase the collective remanent magnetization as compared to when the nanocubes were randomly ordered. However, each nanocube still behaves as a single magnetic unit. Since not all the nanocubes' ⟨100⟩ axes are aligned perfectly with the long axis of the strand, the individual nanocube's magnetic moment may temporarily align with the direction of the applied field when forming the aligned chain but then settle back to a certain degree to its preferred magnetocrystalline anisotropy's ⟨100⟩ axis, still yielding a low net remanence for the MNC strand.

In contrast to the MNCs, the 0.5 vol% aligned chains experience much weaker interactions among all the investigated samples. These weaker interactions are expected to result in increased values of H_c and M_r/M_s. As anticipated, the chain samples exhibit significantly higher remanent magnetization in the hysteresis loop compared to the aligned MNC strands, indicating an improvement in magnetic anisotropy. This is due to the fusing together of nanocubes as they form the long chain, which then acts as a single magnetic unit and maintains a stable remanent magnetization along the direction of the previously applied magnetic field. These results validate the superior performance of chains as magnetic fillers in microactuators.

2.4. Magnetic Properties as a Function of Volume Percentage

To maximize magneto-mechanical transduction, magnetic actuators must maximize their remanent magnetic moment per unit volume. Higher concentrations of magnetic filler, however, can have two major drawbacks. The first is the mechanical stiffening of a soft matrix. The second is that inter-cube/chain dipolar interactions tend to reinforce the magnetization only if the interaction distance along the length direction (head to tail of the magnets) is reduced, but tend to counteract the desired magnetization orientation if the interaction distance along the width, or lateral, direction (head to head of the magnets) is reduced. The latter encourages an antiparallel magnetization state with net zero remanent magnetization. At high concentrations, both magnetic interactions are present, which makes their effects on the net magnetization hard to deconvolve. Here, we examined the role of lateral distance between cubes/chains (representing the concentration of the filler in the matrix) on the magnetic properties of the collective magnetic system. The external field was kept constant at 100 mT as the lateral distance was tuned by the volume percentage of the nanochain solution.

The aligned chain samples were prepared with concentrations of 2, 4, 6, 8, and 10 vol% (**Figure 3**A here and Figure S5, Supporting Information), resulting in the lateral distance between chains varying from 10 to 2.5 μm. In **Table 2**, we present a summary of the relationship between volume percentage and the structural characteristics of elongated chains, including lateral distance and aspect ratio. At a concentration of 2 vol%, in Figure 3A, linear structures with a length of 50 μm, width of 0.3 μm, and aspect ratio of ≈167 were formed. When the volume percentage increases to 4 vol%, correlated with decreasing lateral distance, the aspect ratio of the linear structures increases (≈200) but also shows a broader distribution in chain length and width. Surprisingly, the aspect ratio distribution of the chains prepared at a concentration of 6 vol% (lateral distance between chains of 6 μm) becomes narrower with an average of 280, as shown in Figure 3A and Figure S5C, Supporting Information. When the volume percentage continues to increase, the linear structures exhibit not only increased length but also increased width. This leads to a similar aspect ratio as observed in the case with a 6 μm lateral distance (6 vol%). In other words, the aspect ratios of the elongated structures prepared at 6, 8, and 10 vol% are nearly the same.

A higher degree of chain–chain interaction and end-to-end stacking is expected with increasing concentration of nanochain solution (decreasing lateral distance). Magnetostatics dictates that the chains attract or repel one another depending on their positions in a magnetizing field. At low concentrations, small chains are formed quickly and aligned with the applied magnetic field. As the chain concentration increases, small chains have two possible outcomes: they can both connect end to end and form longer chains, or they can attach side by side, which causes the chains to broaden. Once the assembled structure is fixed, the magnetic field can be removed and the chains may then couple ferro- or antiferromagnetically, depending on their lengths, separations, and relative orientations. For the lateral distance between chains larger than 6 μm, the inter-chain interactions are very weak. Under this condition, short chains tend to form longer chains by attaching to the end of one another, rather than aggregating and forming wider chains. Specifically, at a concentration above 6 vol%, individual short chains no longer exist, indicating that chain end-to-end coupling becomes dominant. Although chains of single-nanocube width can be observed at a lateral distance of 6 μm, when the distance between the chains is reduced to 4 μm, some long chains start to aggregate and attach at the sides. As shown in Figure 3A, there is no significant decrease in the lateral distance at a concentration of 10 vol% (lateral distance of 2.5 μm). Instead, two or more chains tend to attach at the side leading to the widening of the agglomerate. Overall, these results suggest that the aspect ratio of the chains depends on the concentration of the nanochain solution and achieves a maximum at 6 vol%.

The middle and the right columns of Figure S5, Supporting Information, show the full magnetic hysteresis loops and respective graphical enlargements. Clear differences in the magnetic response as a function of angle from 0° to 90° (angle taken from the long axis of the chains) provide strong evidence for anisotropy in the chains regardless of the lateral distance between chains. This is not surprising, since the ultra large aspect ratio of the chains should yield a single magnetic easy axis oriented along the chain axis, which is coincident with one of the iron cobalt cube ⟨100⟩ crystallographic axes, thereby combining the effects of both shape and crystalline anisotropy. As expected, the highest remanence is observed parallel to this high-anisotropy axis along the length of the chain. However, unlike the earlier

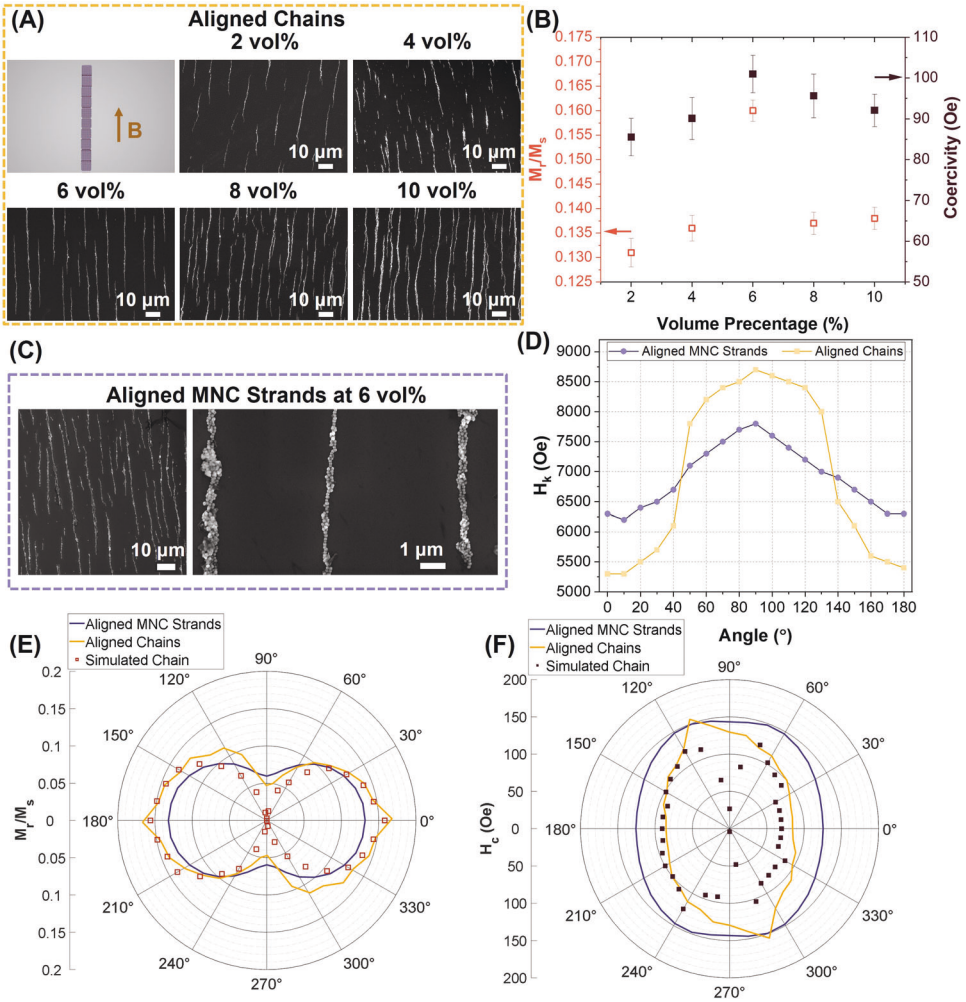

Figure 3. A) SEM images for aligned chain samples as a function of volume percentage: 2 vol%, 4 vol%, 6 vol%, 8 vol%, and 10 vol%. B) Normalized remanence and coercivity of aligned chain samples as a function of volume percentage. C) SEM images for the aligned nanocube sample prepared at 6 vol%. D) Experimental angular dependence of the anisotropic field for magnetically-aligned nanocube (6 vol%) and chain(6 vol%) samples; and polar plots of the (E) normalized remanent magnetization and F) coercivity of the corresponding samples along with the simulated results for the chain sample.

characterization of the highly-concentrated, aligned nanochains, the hysteresis loops of measured samples with well-defined lateral distances do not follow the Stoner–Wohlfarth single-domain magnetization switching model along the chain, since the hysteresis loop perpendicular to the chain axis is not anhysteretic, suggesting the chain is not entirely single domain.

Moreover, in contrast to M_r, the highest coercivity is observed along directions neither parallel nor perpendicular to the chain axis. Specifically, higher energy needs to be overcome to effect a reversal of the magnetization when the field is applied at an angle to the magnetic axes. Imperfect alignment of both the MNCs and their magnetizations within the chains can give rise to this effect because the applied field is never simultaneously perpendicular to the easy axis of all the MNCs. Instead, it is offset from this direction for a subset of MNCs, and this results in the observed enhanced coercivity along the off-chain axis.

Figure 3B summarizes the volume percentage dependence of the normalized remanence, M_r/M_s, and coercivity, H_c. Both properties exhibit one maxima at the volume concentration of 6 vol%. The M_r/M_s ratio appears to decrease significantly above and below 6 vol%. The low remanence at low concentrations is directly due to the lower effective shape anisotropy corresponding to the chain length/width aspect ratio. For a better understanding of the magnetic configuration, we have investigated elongated chains by atomic (AFM) and magnetic force (MFM) microscopy. As the volume percentage is increased to 6 vol%, short chains experience strong ferromagnetic-like coupling toward each other and combine to form longer chains with higher effective anisotropy and higher remanent magnetization (shown in the MFM image of Figure S7, Supporting Information). The decrease in remanence at higher concentrations results from the antiferromagnetic dipolar interaction. More specifically, when the magnetic field is removed, the relatively short lateral distance between chains (at high volume fractions) causes their magnetizations to prefer an antiparallel alignment (shown in the MFM image of Figure S8, Supporting Information), so as to reducetheir

Table 2. Summary of the relationship between volume percentage and structural characteristics of elongated chains.

Concentration	2 vol%	4 vol%	6 vol%	8 vol%	10 vol%
Lateral distance	10 μm	7.5 μm	6 μm	4 μm	2.5 μm
Aspect ratio	167	200	280	280	280

magnetostatic energy. The cause for the peak coercive field at 6 vol% is perhaps less clear. When the short chains combine to form longer chains at higher concentrations, the higher coercivity seen in these longer chains is likely due to the fact that the nodes where the short chains link together serve as pinning points in the magnetization reversal process. Longer chains would therefore result in more pinning cites and higher coercivity. For volume percentages higher than 6 vol%, however, the small lateral distance causes higher inter-chain interaction, resulting in lower H_c.[53] Since 6 vol% achieves the highest remanent magnetization and coercivity, this volume percentage should be considered optimal, and any additional filler added to the soft magnetic actuator should be avoided since it would not only reduce the remanent magnetization and coercivity but also increase the stiffness of the elastomer matrix.

2.5. Enhanced Magnetic Anisotropy in Chains

Most technological applications, including soft magnetic actuators, rely on the magnetic anisotropy energy to determine the initial orientation of the magnetization with respect to the device structure and to provide a stable magnetization direction throughout device operation. To demonstrate the superiority of chains over MNC strands for device applications, we investigated the strength of their magnetic anisotropy as a function of the angle in the aligned samples of the *ideal volume concentration of 6 vol%*, as determined in the previous section. We first prepared the 6 vol% aligned MNC sample, which formed multi-nanocube-wide strands, as shown in Figure 3C. This observation is consistent with studies in the literature,[24,55–57] where MNCs, upon application of an external field, tend to aggregate into irregularly shaped, broad (tens of microns in width) strands along the field direction. *M–H* loops as a function of angle are presented in Figure S6, Supporting Information. These MNC strands exhibit lower remanence along the easy axis than do the aligned chains previously discussed. Although MNC strands exhibit 1D features at the microscale and yield a net magnetic anisotropy globally, they have relatively disordered 3D structures at the nanoscale. Due to the short range disorder and random orientation of the crystal axes of the small MNC building blocks, the agglomerated MNC strands have lower magnetic anisotropy compared with the magnetic nanochains. In contrast to MNCs, chain assemblies exhibit a relatively more ordered structure and higher cohesion, which might confer enhanced mechanical stability.[58,59]

We compared the experimental *M–H* curve measurement results as a function of angle for the nanochains and the aligned MNC strands, both at the same volume percentage of magnetic content (6 vol%). As expected, the anisotropy field (H_k), representing the magnetic field at which magnetization saturates, is strongest in the direction orthogonal to the magnetic easy axis. As seen in Figure 3D, H_k exhibits a clearly sinusoidal trend, being much larger at 90° than at 0°. Compared to the nanochain sample, the MNC strands have a more muted trend, with a smaller variation in H_k between the easy and hard axis directions, confirming the conclusion that these strands have lower anisotropy than the nanochains. The polar plot of the normalized remanent magnetization for each sample consists of the characteristic dumbell shape expected from uniaxial anisotropic samples, with maximum remanence along the 0° and 180° directions. This maximum value corresponds to $M_r/M_s = 0.17$ for the chain sample, which is higher than the $M_r/M_s = 0.13$ for the lower-anisotropy nanocube sample.

Micromagnetic simulations of the nanochain magnetic behavior, as described in the Supporting Information, were utilized to corroborate the experimental *M–H* curve measurement results for the chains as a comparison with the aligned MNC strands. Angle-dependent hysteresis simulations were carried out to assess the magnetic behavior of individual isolated magnetic chains, that is, chains without interactions from nearest neighbors. This approach disregards interactions, providing a useful approximation of the real systems (with 6 vol% concentration) being investigated. This is valid because the remanence of a pair of chains remains similar to that of isolated chains when the lateral distance between chains exceeds 3 μm, as illustrated in Figure S11, Supporting Information. It is important to emphasize that the fact the simulation result for the nanochain sample replicates the experimental data with some accuracy reinforces the understanding that the 6 vol% sample is the most ideal concentration, having the proper length to induce a large shape anisotropy and remanent magnetization but being far enough from neighbors to experience little to no antiferromagnetic-like coupling. In Figure 3E the simulations overlap with the experimental data for magnetic remanence in the parallel configuration (for applied field angles ranging from 0° to 45°), and slightly underestimate M_r/M_s in the perpendicular configuration (from 45° to 90°). The discrepancy between the simulated and experimental M_r/M_s values might be ascribed to the misalignment of the building blocks with respect to the chain axis in the experimentally-synthesized structures. Furthermore, to understand the magnetization reversal behavior, the coercive field as a function of angle was also extracted from the simulation, as shown in Figure 3F. The simulated remanent magnetization state illustrated in Figure S9, Supporting Information, provides evidence for the interpretation that the magnetization is non-uniform throughout the nanochain at zero field, which would result in complex magnetization reversal behavior and large coercivity, especially at an angle to the main axes, explaining the maximum coercive field at an off-axis angle.

Although the major hysteresis loop measurements are powerful and sufficient to describe a magnetic structure in terms of the global behavior, they fail to fully describe complex magnetic nanostructure interactions. A comprehensive insight into the qualitative and quantitative interpretation of interactions between neighboring elements is necessary. A simple technique to investigate these interactions is using FORC. These curves offer information about the distribution of both switching and interaction fields. By studying the correlation between structural arrangements and interactions, we can further investigate the influence of interaction on magnetic anisotropy in these samples.

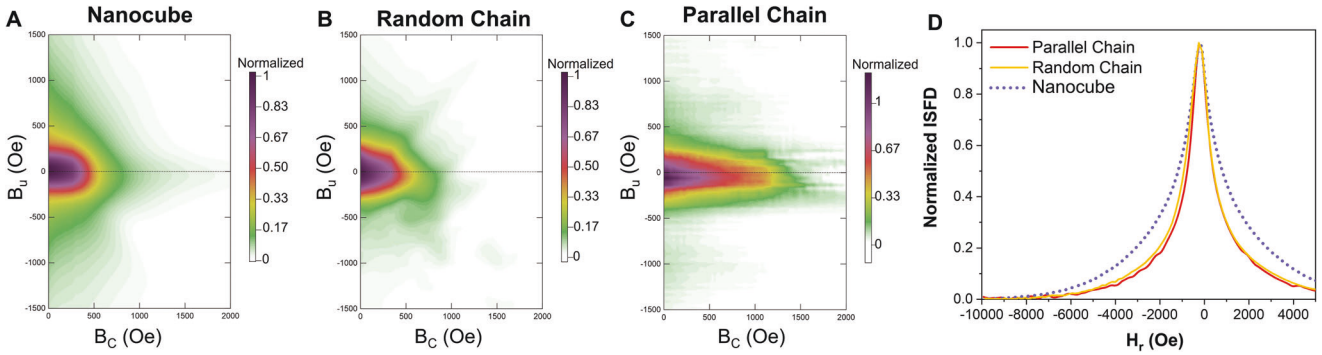

Figure 4. FORC diagrams for randomly-oriented A) nanocube, (B) chain, and C) aligned chain samples each at 6 vol% concentration. D) Irreversible switching field distributions (ISFD) for each of the three samples.

Figure 4 shows the 2D FORC diagrams for different samples. (More details on the FORC measurements and analysis are presented in the Supporting Information.) In all three sample cases, there is a distribution in both interaction (B_u, vertical axis) and switching (B_c, horizontal axis) fields, with the former being due to inter-element interactions, and the latter to different nanostructure elements switching at different applied field strengths.

In a FORC diagram, entirely closed contours are typically considered to be a fingerprint of single-domain particles, whereas open contours that diverge at the B_u axis are a fingerprint of multi-domain behavior.[60] Since the results shown in Figure 4 demonstrate open contours in all three cases, multi-domain behavior can be assumed for each of the samples based upon the conventional interpretation of FORC diagrams. This, once again, suggests that the hysteresis behavior of the samples can not be explained using the simple Stoner–Wohlfarth model and is supported by the simulation result in Figure S9, Supporting Information, which does not exhibit a single domain remanent state in an individual nanochain.

As shown in Figure 4A, the FORC diagram for the randomly-oriented nanocube sample shows typical features for interacting magnetic elements, where a peak is centered at the origin and spreads both vertically and horizontally. The FORC diagram for the randomly-oriented chain sample also shows a pattern similar to that of the nanocube sample, with one important difference—a slightly narrower peak along the interaction field axis (B_u, vertical axis in Figure 4B), which implies that the effective field each magnetic element imposes upon its neighbor is smaller and creates a weaker interaction than in the nanocube-to-nanocube interactions. This can be explained by the relatively small volume of the MNCs, which allows them to be more densely packed than in chains. The larger interactions in the MNC sample can further explain its lower coercivity and remanence compared with those of the randomly-oriented chain sample (Figure 2F). In contrast to the two prior samples, the FORC diagram for the aligned chain sample (Figure 4C) displays an elongated distribution along the coercivity axis, while the distribution along the interaction field axis is only slightly narrower than in the case of the randomly-aligned nanochains. The peak on the interaction field axis (B_u, vertical axis) in the FORC distribution, therefore, narrows as the magnetic ordering of the sample increases, which can suggest that magnetic interactions are becoming less dominant. These results qualitatively support the hypothesis that the random packing of small elements, like nanocubes, yields a higher interaction between the elements but a low anisotropy; but increased order in the system through chain formation and alignment helps to reduce the interaction between neighbors and increase the anisotropy, as expected.

To expand upon this qualitative interpretation of the FORC results, we quantified the behavior by extracting the irreversible switching field distribution (ISFD) for each of the samples. Here, the FORC distributions were projected onto the reversal field H_r axis, as explained in the Supporting Information. As shown in Figure 4C, the aligned FeCo nanochain sample shows the narrowest peak, and the peak broadens for the randomly-oriented FeCo nanochain sample, indicating that the aligned nanochains have a more uniform magnetic response when the applied field is parallel with the chain axis. The nanocube sample has the widest ISFD peak due to the strong nanocube–nanocube interactions that tend to counteract the effect of the applied field.

The reversal field distribution reflects a convolution of not only the individual elements' coercive fields but also their interaction strengths with neighboring structures. In the nanocube case, the distribution in the coercive fields of the individual nanocubes is further exacerbated by the random orientations and distances between the nanocubes that result in varying degrees of coupling interactions and significantly different reversal fields from nanocube to nanocube across the assembly. Thus, the randomness of the arrangement of elements in the assembly broadens the switching field distribution. As the degree of order increases (from randomly-ordered nanocubes to random chains), the coercivity of the individual element increases, making it less susceptible to coupling from other elements.[61] This results in a significantly narrower reversal field distribution for the randomly-ordered chain assembly. Finally, as the degree of order further increases (from random chains to aligned chains), the switching field distribution again decreases, but only slightly. This is believed to be due to the fact that interaction between elements tends to reduce the coercivity,[53] as in the case of the random nanocubes and chains, but when the interaction approaches zero, the value of switching field, H_r, settles to that of the individual element, or the chain in this case, which would correspond to $H_r = -H_c$. However, as seen in Figure 4C, though the interaction field distribution is narrow, the coercive field distribution of the chains is still quite broad, leading to a similar, only slightly

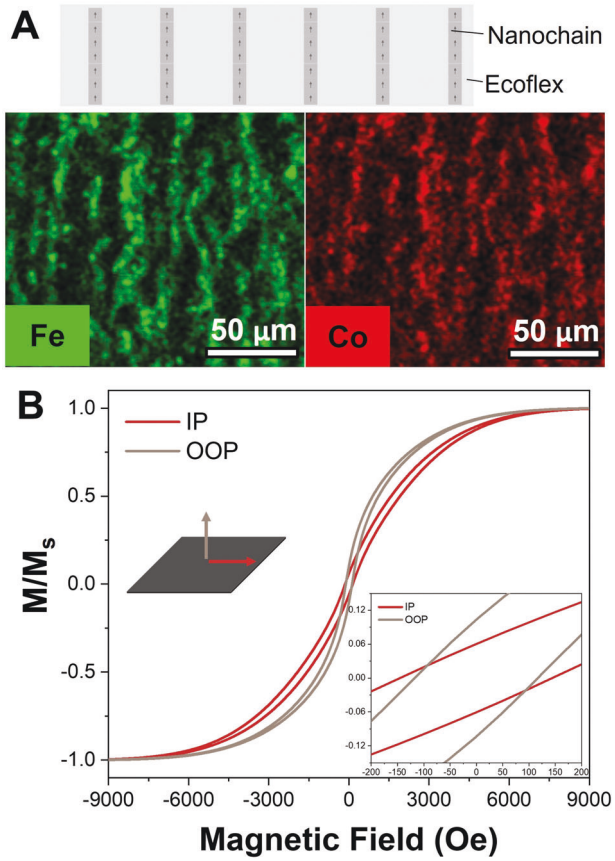

Figure 5. A) The illustrative figure showing the cross-section of the elastomer film and EDS element mappings of cross-section of the elastomer prepared with a 6 vol% nanochain concentration; and B) the IP and the OOP magnetic hysteresis loops for the elastomer (inset: zoomed-in loops from −200 to 200 Oe).

narrower, switching field distribution as in the randomly-oriented chain case.

2.6. Actuator Prototype

2.6.1. Design, Fabrication, and Characterization of Anisotropic Magnetic Elastomer Actuators

As implied by the previous results, the optimal magnetic filler concentration for a soft magnetic actuator was found to be 6 vol%, which gave the highest anisotropy and remanent magnetization, while also yielding the lowest element-to-element interaction. To further verify this finding, we experimentally studied the deformations of the anisotropic magnetic films prepared with different volume fractions (2, 4, 6, 8, and 10 vol%) of magnetic nanochains in the varying magnetic field. The fabrication process of anisotropic magnetic elastomers can be found in the Experimental Section. The as-fabricated elastomers have a thickness of 200 μm.

Figure 5A shows an illustrative image of the cross-section of the elastomer film fabricated with 6 vol%, where chains are oriented perpendicular to the plane of the film. The structural anisotropy was confirmed by EDS mappings of the cross-section of the elastomer. The EDS mappings in Figure 5A depict the expected columnar orientation of the nanochains in the out-of-plane direction of the anisotropic film, corresponding to the direction of the applied field during curing.

The elastomer's deflection was tested in a magnetic field gradient with a custom-built experimental setup. In this setup, the elastomer was securely clamped within a circular cavity of 10 mm diameter. The specifics of the setup and the procedures for measurement are explained in detail in the Supporting Information. Figure S15, Supporting Information, shows the mechanical hysteresis loops measured for the anisotropic elastomers with different volume percentages. The deflection data shows a distinct trend, indicating that as the volume percentage of nanochains in the films increases, the magneto-responsiveness is initially enhanced, resulting in a more pronounced deflection. Nevertheless, this trend levels off at 6 vol% and exhibits a slight decrease when the nanochain concentration exceeds this optimal percentage of the total composite volume.

The enhancement in the deflection is very effective at low magnetic fields (e.g., ≈100 μm at 40 mT), about five times that of microparticle-based elastomers having a morphological arrangement in the form of particle strands (≈20 μm at 40 mT).[12] Table S2, Supporting Information, provides a summary of the literature[10,12,62] with similar deflection measurement setups, which entail clamped magnetic elastomers within cavities. One such study using microparticles reported a deflection of 125 μm at an external magnetic field of 210 mT.[10] In a nanoparticle-based elastomer reported by Pirmoradi et al.,[62] the elastomer requires a 160 mT magnetic field to achieve an approximate 110 μm deflection. Compared to these two isotropic magnetic elastomers, we conclude that the anisotropy of our magnetic elastomers is what enables a larger deflection at lower fields.

The magnetic behavior of the optimal (6 vol%) anisotropic film made of nanochains was investigated by measuring magnetization as a function of applied magnetic field in the out-of-plane (OOP) direction (same direction as the previously-used curing field and the magnetic field used during actuation of the films) and compared with the *M*–*H* loop for the in-plane (IP) direction (orthogonal to the nanochain/actuation axis). The magnetic behavior of the elastomer along each direction can be seen to differ in Figure 5B for applied fields smaller than the saturation field of 6 kOe (600 mT). However, the distinct differences in the hysteresis loops observed for applied fields less than 100 Oe (inset in Figure 5B) suggest potential for enhanced actuation along the OOP direction, as desired. Therefore, this concentration was used as the basis for an experimental demonstration of a soft magnetic actuator.

2.6.2. Actuation of Cantilever

To visually exemplify the reprogrammable capabilities of the actuator, a vertical cantilever with two magnetic elastomer panels magnetized OOP was designed, as depicted in **Figure 6**A. The magnetic elastomer panels integrated in the cantilever can be magnetized in opposite or the same directions, leading to varied actuation behavior. For the first set of actuation experiments, the cantilever was mounted vertically on top of an aluminum plate

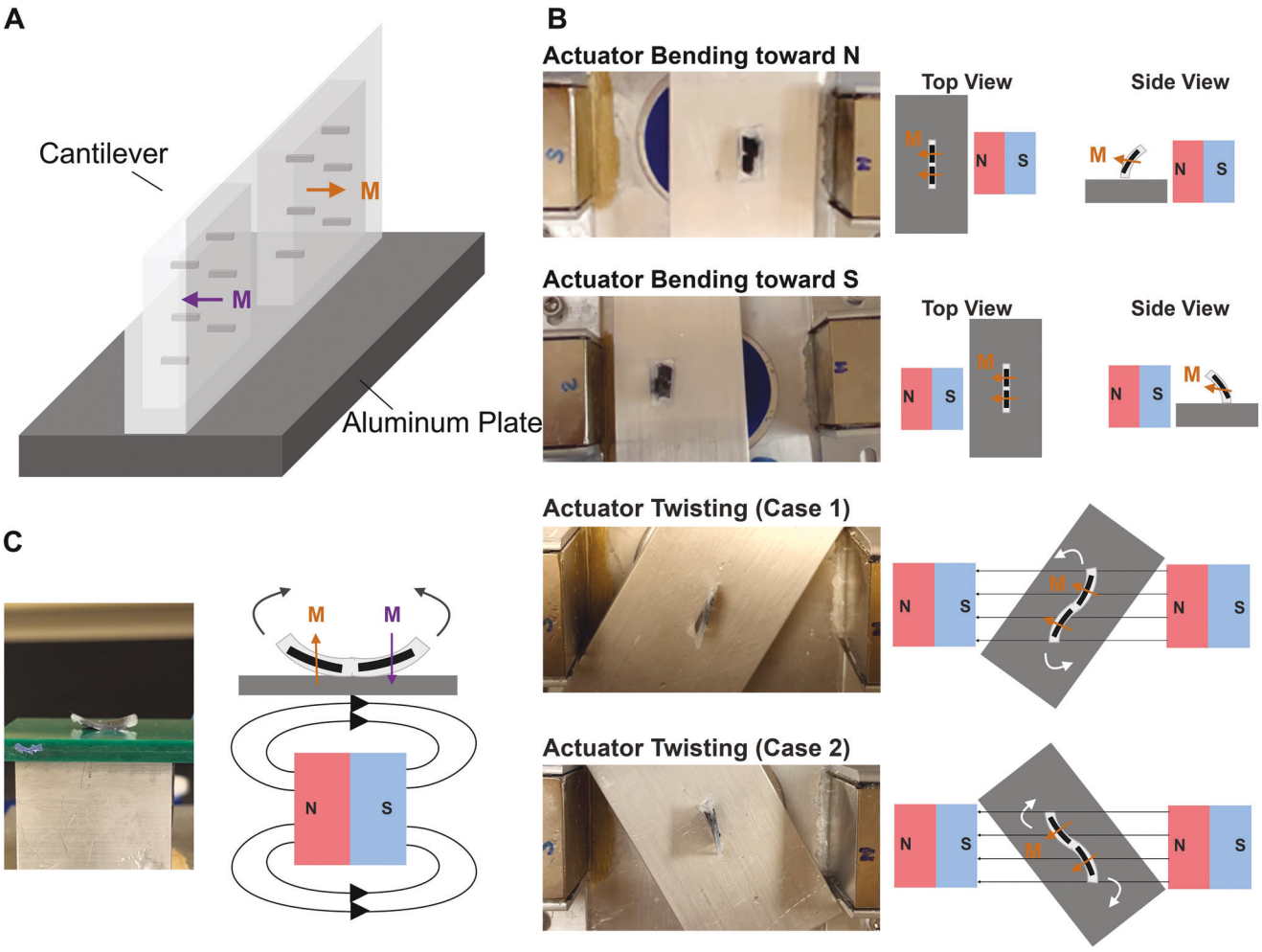

Figure 6. Actuation of elastomer with a 6 vol% nanochain concentration. A) Schematic design of the cantilever made of two panels of elastomers magnetized with opposite directions; B) Left column: Photos of the cantilever deforming in different modes induced by magnetic forces and right column: Schematic illustration of the corresponding deformation mechanisms of the cantilever; and C) Left: Photo of the film performing U-shaped bending induced by magnetic torques, and right: Schematic illustration of the corresponding deformation mechanism of the film.

such that the nanochains inside the elastomer actuator were parallel to the top surface of the plate. The top view of this actuation testbed is shown in the photos of Figure 6B.

Bending and S-shaped twisting actuation modes can be observed in the case when both panels are magnetized along the same direction, by either moving the aluminum plate toward one of the two block magnets on the sides or rotating the aluminum plate about the center axis, respectively. As shown in the video (which can be found in the Supporting Information) and Figure 6B, when moved toward one of the block magnets, the cantilever experiences a field of approximately ±30 mT and gradient of ±10 mT cm^{-1} and bends toward the magnet. When the cantilever approaches either side, the field of ±30 mT (300 Oe) is strong enough to temporarily magnetize both panels in the cantilever along the field direction of the block magnet (as seen from the hysteresis loop in Figure 5B). The bending results from the magnetic force due to the strong field gradient ±10 mT cm^{-1} acting upon the magnetized film ($\vec{F} = \nabla(\vec{m} \cdot \vec{B})$). By rotating the aluminum plate toward either the north or the south side, S-shaped twisting is observed, where the direction of the magnetic field controls the shape of the cantilever. The rotation of the cantilever gives rise to magnetic torques ($\vec{\tau} = \vec{m} \times \vec{B}$) due to a magnetic flux density of 30 mT acting on its magnetization. The cantilever twists into the shape of an S because the magnetic moments in the two panels experience the same torque.

For the set of actuation experiments done when the panels in the film are magnetized in opposite directions, the actuator was laid down flat on top of an acrylic plate such that the nanochains inside the elastomer actuator were perpendicular to the top surface of the plate. The side view of this actuation testbed is shown in Figure 6C. As the actuator is brought closer to the top of the magnet, opposite magnetic torques ($\vec{\tau} = \vec{m} \times \vec{B}$) are exerted on the oppositely-magnetized panels due to the 40 mT flux density acting on them. The actuator bends into a U shape. Thus, by programming the orientation and the strength of the external magnetic field, a variety of actuation modes ranging from cantivlever bending to both S-shaped twisting and U-shaped bending of the actuators can be achieved to develop complex

deformations for use in magnetic-actuator systems such as haptics and soft robotics.

3. Conclusion

In summary, we presented detailed experiments on the verification of enhancement in magnetic properties in microscale collectives of 1D nanochains and MNCs. This study reveals that the synthesized nanochains can be aligned at an optimized concentration to increase their net remanent magnetization and anisotropy, which improves the device performance when incorporated into a matrix, such as an elastomer matrix for a soft magnetic actuator. In contrast, MNCs are also able to form elongated strands but only show a moderate increase in the remanent magnetization. Furthermore, the successful formation of single-nanocube-wide 1D nanochain arrays having controlled lateral distance between chains (ranging from 2.5 to 10 μm) allowed for magnetic measurements to be done as a function of magnetic filler density— a proxy for varying interchain interaction strength. Of these 1D chain arrays, an optimal nanochain density arose to be 6 vol% magnetic concentration, which gave the highest remanent magnetization and coercivity.

The magnetic anisotropy of the nanochains at 6 vol% was compared with the reference case, that is, the MNC strands formed under the same volume percentage. These results clearly demonstrate that 1D nanochain arrays can produce a net uniaxial anisotropy energy that well exceeds the strength that of MNC strands (those most commonly formed in the literature by applying a field to align MNCs), a conclusion that is also supported by FORC measurements. A soft magnetic actuator, fabricated using the optimal 6 vol% magnetic filler concentration, achieved a relatively large mechanical response, with a deflection of up to 0.4 mm at very small magnetic fields of <100 mT. Thus, results from this research elucidate the impact of lateral distance between magnetic elements on their collective magnetic behavior. We have shown that only by having the proper concentration of magnetic content can the net magnetic remanence and anisotropy of the collective magnetic system be increased and the desired magneto-mechanical transduction (or other forms of transduction) be maximized. With such optimizations, future devices and actuators, like the soft actuators demonstrated here, can be scaled down to sub-millimeter dimensions while still achieving large force densities.

4. Experimental Section

Synthesis of the FeCo Nanostructures: Nanochains were synthesized using a highly concentrated polyol method, reported in detail elsewhere.[47] First, $FeCl_2$ (1.2 mmol, VWR International) and $Co(Ac)_2 \cdot 4\,H_2O$ (0.4 mmol, VWR International) were added to 5 mL of ethylene glycol (obtained from Fisher Scientific) and ultrasonicated for 30 min to achieve complete dissolution. In a 50-mL three-neck round bottom flask, 64 mmol NaOH pellets (VWR International) were dissolved in 20 mL of ethylene glycol, which was heated to 130°C and stirred at a constant rate of 300 rpm. Subsequently, the metal precursor solution was injected into the flask and refluxed at 130°C for 10 min. N_2 flowed continuously through the flask during the synthesis to prevent oxidation. Finally, the products were separated by a magnet and washed with a two-step process, first with distilled water (Fisher Scientific), followed by absolute ethanol (Fisher Scientific), and then washed again a second time with the same two-step process. Nanocubes were prepared under the same experimental conditions as the nanochains except that a total volume of 100 mL of ethylene glycol was used instead of 25 mL.

Structural and Magnetic Characterization: Dilute suspensions were prepared with varied concentrations of magnetic nanostructures, ranging from 0.5 to 10 vol%, by adding a measured quantity of the as-synthesized FeCo into ethanol and ultrasonicating for 30 min to ensure a homogenous solution. 10 μL aliquots of these suspensions were then dropped-cast onto silicon substrates (5×5 mm^2) for subsequent experimental characterization of the random arrangement of chains or nanocubes. Samples with aligned chains or nanocubes were prepared with the same protocol but were dropped-cast onto silicon substrates under a magnetic field of 100 mT. The schematic explanation of the preparation process is shown in Figure S2, Supporting Information. SEM images were taken using a Zeiss-Gemini-500 microscope with an attached EDS. The EDS was used for compositional analysis as well as confirmation of the uni-directional alignment of the FeCo nanostructures inside the polymer matrix, in the latter part of this work. TEM bright-field images and a SAED pattern were acquired on an FEI Tecnai 12 BioTwin TEM. The crystal structure of the magnetic samples was characterized using XRD (Bruker D8 Advance ECO). Magnetic measurements were performed with a vibrating sample magnetometry system (8600 Series VSM from Lakeshore) to record M versus H hysteresis loops at room temperature with a maximum applied field of ±15000 Oe for all samples.

Actuator Prototype Fabrication:: The anisotropic magnetic-chain-elastomer composite was prepared by incorporating 6 vol % of FeCo chains into a mixture of silicone elastomer (Smooth-On, Ecoflex 00-30), where parts A and B were mixed in a 1:1 ratio. Figure S13, Supporting Information, schematically shows the fabrication process. First, FeCo nanochains (with a volume concentration of 6% of the final mixed components) were mixed manually into Ecoflex Part A. The resulting mixture was ultrasonicated in a bath (40 kHz and 180 W) at room temperature for 2 min, allowing them to be well dispersed into the organic matrix. Ecoflex Part B was then added, and the final solution was mixed manually for a few seconds. The composite mixture was immediately transferred to a custom-made aluminum mold, which had been pre-sprayed with Ease Release 200. The mold was kept under vacuum for 2 min in a desiccator to eliminate any air bubbles entrapped in the mixture. To define the orientation of the FeCo chains out-of-plane, through the thickness of the elastomer, the mold (with the mixture inside) was placed along the *xy*-plane in a uniform 100 mT magnetic field along the *z*-direction of an electromagnet. Once the composite had fully cured (≈4 h at room temperature), the elastomer was removed from the mold and cut in half along its width. The resulting elastomer had a thickness of about 200 μm. The two pieces of the elastomer were placed side-by-side with opposite chain magnetization directions and bonded with additional silicone elastomer to make up the final actuator.

Supporting Information

Supporting Information is available from the Wiley Online Library or from the author.

Acknowledgements

This work made use of the Cornell Center for Materials Research Shared Facilities which was supported through the NSF MRSEC program (DMR-1719875). This work was performed in part at the Cornell NanoScale Facility, a member of the National Nanotechnology Coordinated Infrastructure (NNCI), which was supported by the National Science Foundation (Grant NNCI-2025233). This material is based upon work supported by the National Science Foundation under Grant No. 2030207. Any opinions, findings, and conclusions or recommendations expressed in this material are those of the authors and do not necessarily reflect the views of the National Science Foundation.

Conflict of Interest

The authors declare no conflict of interest.

Data Availability Statement

The data that support the findings of this study are available from the corresponding author upon reasonable request.

Keywords

magnetic actuation, magnetic anisotropy, magnetic elastomers, magnetic interactions, magnetic nanochains

Received: May 17, 2023
Revised: September 7, 2023
Published online:

[1] S. W. Kwok, S. A. Morin, B. Mosadegh, J.-H. So, R. F. Shepherd, R. V. Martinez, B. Smith, F. C. Simeone, A. A. Stokes, G. M. Whitesides, *Adv. Funct. Mater.* **2014**, *24*, 2180.
[2] Y. Kim, X. Zhao, *Chem. Rev.* **2022**, *122*, 5317.
[3] J. J. Zárate, H. Shea, *IEEE Trans. Haptics* **2016**, *10*, 106.
[4] L. Cestarollo, S. Smolenski, A. El-Ghazaly, *ACS Appl. Mater. Interfaces* **2022**, *14*, 19002.
[5] R. M. Erb, J. J. Martin, R. Soheilian, C. Pan, J. R. Barber, *Adv. Funct. Mater.* **2016**, *26*, 3859.
[6] S. M. Montgomery, S. Wu, X. Kuang, C. D. Armstrong, C. Zemelka, Q. Ze, R. Zhang, R. Zhao, H. J. Qi, *Adv. Funct. Mater.* **2021**, *31*, 2005319.
[7] A. K. Hoshiar, S. Jeon, K. Kim, S. Lee, J.-y. Kim, H. Choi, *Micromachines* **2018**, *9*, 617.
[8] L. Pancaldi, P. Dirix, A. Fanelli, A. M. Lima, N. Stergiopulos, P. J. Mosimann, D. Ghezzi, M. S. Sakar, *Nat. Commun.* **2020**, *11*, 6356.
[9] X. Hu, I. C. Yasa, Z. Ren, S. R. Goudu, H. Ceylan, W. Hu, M. Sitti, *Sci. Adv.* **2021**, *7*, 23eabe8436.
[10] W. Wang, Z. Yao, J. C. Chen, J. Fang, *J. Micromech. Microeng.* **2004**, *14*, 1321.
[11] S. Kashima, F. Miyasaka, K. Hirata, *IEEE Trans. Magn.* **2012**, *48*, 1649.
[12] S. Marchi, A. Casu, F. Bertora, A. Athanassiou, D. Fragouli, *ACS Appl. Mater. Interfaces* **2015**, *7*, 19112.
[13] B. Han, Z.-C. Ma, Y.-L. Zhang, L. Zhu, H. Fan, B. Bai, Q.-D. Chen, G.-Z. Yang, H.-B. Sun, *Adv. Funct. Mater.* **2022**, *32*, 2110997.
[14] R. Bayaniahangar, S. B. Ahangar, Z. Zhang, B. P. Lee, J. M. Pearce, *Sens. Actuators, B* **2021**, *326*, 128781.
[15] R. Lussier, Y. Giroux, S. Thibault, D. Rodrigue, A. M. Ritcey, *Polym. Adv. Technol.* **2020**, *31*, 1414.
[16] H. Song, H. Lee, J. Lee, J. K. Choe, S. Lee, J. Y. Yi, S. Park, J.-W. Yoo, M. S. Kwon, J. Kim, *Nano Lett.* **2020**, *20*, 5185.
[17] Z. Wu, Q. Wang, J. Huang, Y. Yue, D. Chen, Y. Shi, B. Su, *Compos. Sci. Technol.* **2022**, *217*, 109129.
[18] Z. Li, F. Yang, Y. Yin, *Adv. Funct. Mater.* **2020**, *30*, 1903467.
[19] S. R. Mishra, M. D. Dickey, O. D. Velev, J. B. Tracy, *Nanoscale* **2016**, *8*, 1309.
[20] B. Mordina, R. K. Tiwari, D. K. Setua, A. Sharma, *J. Phys. Chem. C* **2014**, *118*, 25684.
[21] O. Riou, B. Lonetti, R. P. Tan, J. Harmel, K. Soulantica, P. Davidson, A.-F. Mingotaud, M. Respaud, B. Chaudret, M. Mauzac, *Angew. Chem.* **2015**, *127*, 10961.
[22] Q. Zhang, B. Peng, H. Li, J. Sun, *Soft Mater.* **2018**, *16*, 220.
[23] S. H. Kwon, C. J. Lee, H. J. Choi, K. H. Chung, J. H. Jung, *Smart Mater. Struct.* **2019**, *28*, 045012.
[24] E. Myrovali, K. Papadopoulos, I. Iglesias, M. Spasova, M. Farle, U. Wiedwald, M. Angelakeris, *ACS Appl. Mater. Interfaces* **2021**, *13*, 21602.
[25] J. Kim, S. E. Chung, S.-E. Choi, H. Lee, J. Kim, S. Kwon, *Nat. Mater.* **2011**, *10*, 747.
[26] A. Tokarev, J. Yatvin, O. Trotsenko, J. Locklin, S. Minko, *Adv. Funct. Mater.* **2016**, *26*, 3761.
[27] T. Davidson, in *Functional Fillers for Plastics* (Ed: M. Xanthos), Wiley, Hoboken, NJ **2005**, pp. 317–337.
[28] B. Duong, H. Khurshid, P. Gangopadhyay, J. Devkota, K. Stojak, H. Srikanth, L. Tetard, R. A. Norwood, N. Peyghambarian, M.-H. Phan, J. Thomas, *Small* **2014**, *10*, 2840.
[29] S. Mørup, *Europhys. Lett.* **1994**, *28*, 671.
[30] O. Petracic, X. Chen, S. Bedanta, W. Kleemann, S. Sahoo, S. Cardoso, P. Freitas, *J. Magn. Magn. Mater.* **2006**, *300*, 192.
[31] J. Mohapatra, M. Xing, J. P. Liu, *Materials* **2019**, *12*, 3208.
[32] D. Peddis, K. Trohidou, M. Vasilakaki, G. Margaris, M. Bellusci, F. Varsano, M. Hudl, N. Yaacoub, D. Fiorani, P. Nordblad, R. Mathieu, *Sci. Rep.* **2021**, *11*, 7743.
[33] E. H. Sánchez, M. Vasilakaki, S. S. Lee, P. S. Normile, M. S. Andersson, R. Mathieu, A. López-Ortega, B. P. Pichon, D. Peddis, C. Binns, P. Nordblad, K. Trohidou, J. Nogués, J. A. De Toro, *Small* **2022**, *18*, 2106762.
[34] E. Wetterskog, C. Jonasson, D.-M. Smilgies, V. Schaller, C. Johansson, P. Svedlindh, *ACS Nano* **2018**, *12*, 1403.
[35] M. Varón, M. Beleggia, T. Kasama, R. Harrison, R. E. Dunin-Borkowski, V. F. Puntes, C. Frandsen, *Sci. Rep.* **2013**, *3*, 1234.
[36] B. J. Stottlemire, J. D. Miller, J. Whitlow, S. G. Huayamares, P. Dhar, M. He, C. J. Berkland, *Adv. Mater. Technol.* **2021**, *6*, 2001099.
[37] F. J. Vazquez-Perez, C. Gila-Vilchez, J. Duran, A. Zubarev, L. A. de Cienfuegos, L. Rodriguez-Arco, M. T. Lopez-Lopez, *Polymer* **2021**, *230*, 124093.
[38] J. Seifert, S. Roitsch, A. M. Schmidt, *ACS Appl. Polym. Mater.* **2021**, *3*, 1324.
[39] C. Li, G. C. Lau, H. Yuan, A. Aggarwal, V. L. Dominguez, S. Liu, H. Sai, L. C. Palmer, N. A. Sather, T. J. Pearson, D. E. Freedman, P. K. Amiri, M. O. De La Cruz, S. I. Stupp, *Sci. Rob.* **2020**, *5*, eabb9822.
[40] R. A. Landa, P. Soledad Antonel, M. M. Ruiz, O. E. Perez, A. Butera, G. Jorge, C. L. Oliveira, R. M. Negri, *J. Appl. Phys.* **2013**, *114*, 213912.
[41] J. Jia, J. C. Yu, Y.-X. J. Wang, K. M. Chan, *ACS Appl. Mater. Interfaces* **2010**, *2*, 2579.
[42] M. Agrawal, B. Rana, A. Barman, *J. Phys. Chem. C* **2010**, *114*, 11115.
[43] D. Toulemon, M. V. Rastei, D. Schmool, J. S. Garitaonandia, L. Lezama, X. Cattoën, S. Bégin-Colin, B. P. Pichon, *Adv. Funct. Mater.* **2016**, *26*, 2454.
[44] M. V. Rastei, V. Pierron-Bohnes, D. Toulemon, C. Bouillet, A. Kákay, R. Hertel, E. Tetsi, S. Begin-Colin, B. P. Pichon, *Adv. Funct. Mater.* **2019**, *29*, 1903927.
[45] M. Krajewski, M. Tokarczyk, S. Lewińska, K. Brzózka, K. Bochenek, A. Ślawska-Waniewska, *Materials* **2021**, *14*, 4748.
[46] P. Laha, B. K. Mahato, R. Gayen, S. Datta, R. S. Rawat, *Appl. Phys. A* **2022**, *128*, 394.
[47] Y. Chen, A. El-Ghazaly, *Small* **2022**, *19*, 2205079.
[48] J. Liu, K. Wu, J.-P. Wang, *AIP Adv.* **2016**, *6*, 056126.
[49] M.-S. Jang, M. S. Chang, Y.-t. Kwon, S. Yang, J. Gwak, S. J. Kwon, J. Lee, K. Song, C. R. Park, S. B. Lee, B. Park, J. W. Jeong, *Nanoscale* **2021**, *13*, 12004.
[50] V. Vadillo, A. Gómez, J. Berasategi, J. Gutiérrez, M. Insausti, I. G. de Muro, J. S. Garitaonandia, A. Arbe, A. Iturrospe, M. M. Bou-Ali, J. M. Barandiarán, *Soft Matter* **2021**, *17*, 840.
[51] J. Liu, K. Wu, S. He, J. Bai, Y.-H. Xu, J.-P. Wang, *ACS Appl. Nano Mater.* **2021**, *4*, 9382.
[52] J. G. Ovejero, D. Cabrera, J. Carrey, T. Valdivielso, G. Salas, F. J. Teran, *Phys. Chem. Chem. Phys.* **2016**, *18*, 10954.

[53] D. Kechrakos, K. Trohidou, *J. Magn. Magn. Mater.* **2003**, *262*, 107.
[54] R. Tan, J. Lee, J. Cho, S. Noh, D. Kim, Y. Kim, *J. Phys. D: Appl. Phys.* **2010**, *43*, 165002.
[55] Y. Sahoo, M. Cheon, S. Wang, H. Luo, E. Furlani, P. Prasad, *J. Phys. Chem. B* **2004**, *108*, 3380.
[56] G. Singh, H. Chan, A. Baskin, E. Gelman, N. Repnin, P. Král, R. Klajn, *Science* **2014**, *345*, 1149.
[57] S. M. Taheri, M. Michaelis, T. Friedrich, B. Förster, M. Drechsler, F. M. Römer, P. Bösecke, T. Narayanan, B. Weber, I. Rehberg, S. Rosenfeldt, S. Förster, *Proc. Natl Acad. Sci. USA* **2015**, *112*, 14484.
[58] V. Håkonsen, G. Singh, P. S. Normile, J. A. De Toro, E. Wahlström, J. He, Z. Zhang, *Adv. Funct. Mater.* **2019**, *29*, 1904825.
[59] V. Håkonsen, G. Singh, J. A. De Toro, P. S. Normile, E. Wahlström, J. He, Z. Zhang, *Adv. Sci.* **2021**, *8*, 2002683.
[60] B. Dodrill, P. Ohodnicki, M. McHenry, A. Leary, *MRS Adv.* **2017**, *2*, 2669.
[61] S. E. Ilse, F. Groß, G. Schütz, J. Gräfe, E. Goering, *Phys. Rev. B* **2021**, *103*, 024425.
[62] F. N. Pirmoradi, L. Cheng, M. Chiao, *J. Micromech. Microeng.* **2009**, *20*, 015032.